Scaling and dynamics of sphere and disk impact into granular media

Daniel I. Goldman*
School of Physics, Georgia Institute of Technology, Atlanta, Georgia 30332, USA

Paul Umbanhowar
Department of Mechanical Engineering, Northwestern University, Evanston, Illinois 60208, USA

(Received 25 September 2007; published 29 February 2008)

Direct measurements of the acceleration of spheres and disks impacting granular media reveal simple power law scalings along with complex dynamics which bear the signatures of both fluid and solid behavior. The penetration depth scales linearly with impact velocity while the collision duration is constant for sufficiently large impact velocity. Both quantities exhibit power law dependence on sphere diameter and density, and gravitational acceleration. The acceleration during impact is characterized by two jumps: a rapid, velocity-dependent increase upon initial contact and a similarly sharp depth-dependent decrease as the impacting object comes to rest. Examination of the measured forces on the sphere in the vicinity of these features leads to an experimentally based granular force model for collision. We discuss our findings in the context of recently proposed phenomenological models that capture qualitative dynamical features of impact but fail both quantitatively and in their inability to capture significant acceleration fluctuations that occur during penetration and which depend on the impacted material.

DOI: 10.1103/PhysRevE.77.021308 PACS number(s): 45.70.−n, 83.80.Fg, 47.50.−d, 46.35.+z

I. INTRODUCTION

Collisions with complex particulate materials occur in diverse situations ranging from asteroid impact [1] to the penetration of a running crab's leg into beach sand [2]. Accordingly, collisions with granular media have long been investigated [3], and, like many areas of granular research, are being actively explored today in experiment [4–11], simulation [4,12], and theory [5–7,10,13–15]. However, because the physics of such events must account for both fluid- and solidlike behavior during impact, understanding remains limited. No comprehensive continuum theory exists for even the relatively low impact velocity of a rock dropped into beach sand from an outstretched hand.

Recent experiments and simulations of low-velocity ($\lesssim 5$ m/s) impact with granular media have mainly considered the depth to which an object penetrates before stopping. These studies have investigated how the penetration depth scales with various system parameters. Durian and coworkers [15,16] performed experiments at low collision velocities v (the maximum penetration depth was approximately a sphere diameter) on a variety of spheres of differing radii R, sphere density ρ_s, and granular particle density ρ_g and found that the penetration depth d scaled as $d \sim v_c^{2/3}\left(\frac{\rho_s}{\rho_g}\right)^{1/2} R^{2/3}$. de Bruyn and Walsh [5] found a different scaling: $d \sim v_c^{1}\left(\frac{\rho_s}{\rho_g}\right)^{1/2} R^{1/2}$. The latter experiments were conducted at larger impact velocities and with spheres of higher density such that maximum penetration depths were much greater than the sphere diameter $d \gg 2R$. In two-dimensional (2D) disk simulations, Tsimring and co-workers found that $d \sim v_c^{4/5}\left(\frac{\rho_s}{\rho_g}\right)^{2/5} R^{3/5}$.

Phenomenological models have been proposed to account for experimental results of penetration depth from spheres impacting granular materials in a gravitational field [5,7,10,14,15]. In all models, the force on a vertically falling object impacting a horizontal granular medium is written in the general form

$$m\frac{d^2z}{dt^2} = -mg + F_d, \tag{1}$$

where m is the mass of the impactor, z is the displacement of the lowest point on the object below the initial free surface of the grains, g is the gravitational acceleration, and F_d is the drag force due to the presence of the granular medium. Impact models typically represent the drag force as the sum of two terms:

$$F_d = F_z + \alpha v^2, \tag{2}$$

where $v = dz/dt$, α is a drag coefficient, and F_z is posited to be a frictional or hydrostatic term with different proposed forms [14,15] depending on the impact regime and impactor geometry. For example, the authors of [14] assume that an impacting sphere experiences hydrostaticlike forces, basing their arguments on experiments of [17] in which the force on a flat intruder moving at a low constant velocity increases linearly with depth below the free surface. They argue that F_z for shallow impact increases as $F_z = 2\eta\rho_g g z^2 R$, with η a parameter dependent on grain properties (e.g., angle of repose) and ρ_g. For deep impact, the free surface is assumed to move along with the sphere such that the bottom of the object is always a fixed distance z_0 below the local free surface; thus F_z approaches a constant with value $F_z = 2\eta\rho_g g z_0^2 R$.

Durian and co-workers [15] fitted penetration depth scaling data from experiment to derive a functional form for the frictional drag in the shallow penetration regime such that

$$F_z = mg + mg[3(z/d_0)^2 - 1]\exp(-2|z|/d_1), \tag{3}$$

*daniel.goldman@physics.gatech.edu; URL: http://www.physics.gatech.edu/goldman/

where d_0 is the penetration depth for an object impacting the surface with initial collision velocity $v_c=0$, and $d_1=m/\alpha$. These two parameters are independent of v_c. Similar to the model of Tsimring and Volfson [14], Eq. (3) also scales like z^2 for $z \ll D$, and approaches a constant (mg) for sufficiently large impact depth. Recently Durian and co-workers [18] proposed that a linear $F(z)$ (similar to the model proposed in [19]) provides a better fit.

To summarize, the granular medium is modeled by a force law with a hydrodynamic drag term proportional to the square of the velocity (which dominates at high velocity and thus deep penetration) and a term that accounts for a depth-dependent static resistance force, which dominates at low speeds and thus shallow penetration depths. Other studies have proposed that the drag force also includes a term linear in velocity [5,6,13]; however, the experiments in [6,13] are in a much higher-velocity regime, 700 m/s, than the regime examined by us and in the other studies cited here, where impact velocities are typically less than 5 m/s.

Since at least 1742 [3] various force laws for granular impact have been proposed and their associated penetration scalings discussed; however, there have been no detailed experimental three-dimensional studies of the *forces* that the colliding object experiences during impact. Measuring and understanding the forces exerted during impact is clearly important, as demonstrated by the recent and surprising experimental finding that a disk comes to rest in a time t_c independent of the initial impact velocity [4]. Fits of position versus time indicated that the acceleration during penetration was constant with magnitude dependent only upon v_c.

Accordingly, we describe here *direct* measurements of the forces exerted on a sphere during penetration of a granular medium. Integrated force measurements show how the penetration depth scales in deep impact experiments (our data most closely follow de Bruyn and Walsh's scaling [5]) while a systematic study of collision duration reveals simple scaling with system parameters. We examine key features of the dynamics using the acceleration data and then use them to guide an examination of the forces at both high and low depths and velocities. Constrained by experimental force data, we propose an equation to describe the forces during granular impact. Finally, we show that while our impact force equation and those referenced above account for some of the features we observe, a wealth of dynamics associated with force fluctuations remains to be understood.

II. EXPERIMENTAL DETAILS

Figure 1 shows a sketch of the experimental apparatus. A MEMS IC accelerometer (Analog Devices ADXL150) with a range of $\pm 50g$'s was mounted on an aluminum plug, which was inserted into a hole or glued to a flat on top of the impactor; a small-diameter tube isolates the accelerometer wires from the granular medium. We note that the small tube does not affect the impact dynamics because the collapsing crater does not contact the tube until well after the impactor has stopped (see top panels of Fig. 1) [20]. We choose acceleration to be positive in the direction opposite gravity. Impactors were dropped into the granular medium from heights

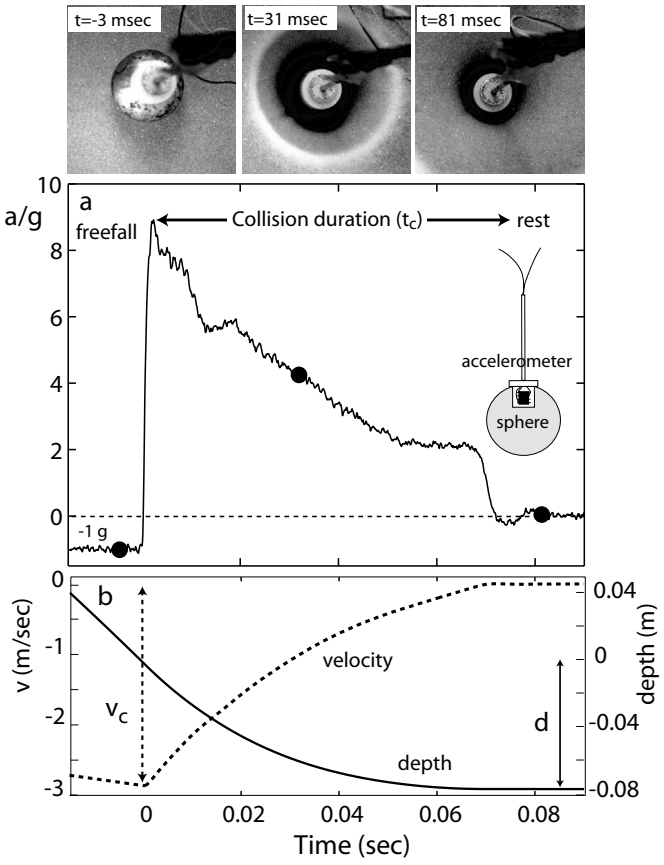

FIG. 1. Three sequential images (overhead view) of an $R=1.91$ cm steel sphere impacting glass beads at $v_c=2.86$ m/s with (a) the acceleration and (b) the velocity and penetration depth of the sphere during the collision [the three dots (●) in (a) correspond with the images]. The depth is defined as the distance from the lowest point on the sphere to the initial free surface of the grains. Also in (a) is a sketch of the instrumented projectile (not to scale) showing a single-axis accelerometer embedded in a sphere.

of $0.01 \sim 2.5$ m with corresponding impact velocities v_c ranging from 0.4 to 7 m/s.

A variety of impactors and granular materials were used (see Tables I and II). Since holes were drilled in some spheres while flats were made on others and the mass of the accelerometer is included in the indicated sphere mass, the "effective" sphere density ρ_s calculated using the masses and radii in the tables does not necessarily match the density of the material of which the sphere is composed. Additionally, six 1.3-cm-radius brass cylinders with different masses were

TABLE I. Granular media.

Material	Size (mm)	ρ_{bulk} (g/cm^3)	θ_r
Glass spheres	0.25–0.42	1.56	23°
Aluminum shot	1×1 (diam. $\times$ length)	1.62	31°
Millet seed	1.2	0.72	28°
Bronze spheres	0.05 and 0.17	5.49	24°

TABLE II. Impactors.

Impactor	Radius (cm)	Mass (g)
Steel sphere	9.5	34
	1.3	83
	1.5	130
	2.0	287
	2.5	531
	3.5	1437
	4.0	2099
	4.5	3055
	5.0	4079
Bronze sphere	1.3	64
	1.9	201
	2.6	518
Nylon sphere	1.25	9
	1.9	18
Bronze disk (5 mm high)	1.0	10

mounted atop the 1.9-cm-radius nylon sphere, which varied ρ_s from 1.88 to 9.31 g/cm^3. Various containers were also employed (see Table III), including a 29-cm-diameter by 40-cm-high PVC bucket, a 25-cm-diameter by 30-cm-high aluminum pot, a 50-cm-diameter by 75-cm-high cardboard barrel, and a 10-cm-diameter by 10-cm-high glass jar. Two different procedures were used to prepare the granular material: (1) The container was vigorously rocked from side to side with decreasing amplitude until the surface was level; (2) a sieve with outer diameter approximately equal to that of the container was placed in the bottom of the container, the material poured in, and the sieve pulled slowly to the surface. Both procedures produced reproducible dynamics. The majority of experiments were conducted with bronze, steel, or nylon spheres or the bronze disk impacting the 0.25–0.42 mm glass beads prepared via rocking in the 30-cm-diameter PVC container filled to a depth of approximately 25 cm. Additionally, to vary the effective gravitational acceleration during impact, an Atwood machine was used to drop the bucket containing the granular material with accelerations ranging from zero to nearly $-g$.

III. IMPACT AND DERIVED QUANTITIES

Figure 1 shows the acceleration, velocity, and position of a sphere colliding with a granular medium. We measure the acceleration directly and integrate to obtain position and velocity. At impact, the acceleration increases rapidly as the material suddenly applies force. The acceleration decreases as the sphere penetrates into the medium and finally comes to rest at a finite penetration depth d in a time t_c. We discuss the details of the acceleration profile in Sec. IV. We begin with a discussion of the dependence of d and t_c on the initial impact velocity v_c as well as sphere density ρ_s, sphere radius R, and gravitational acceleration g.

TABLE III. Containers.

Container	Diameter (cm)	Height (cm)	Wall thickness (cm)
Cardboard barrel	50	75	0.3
PVC bucket	28.5	38	0.3
Aluminum pot	25	30	0.33

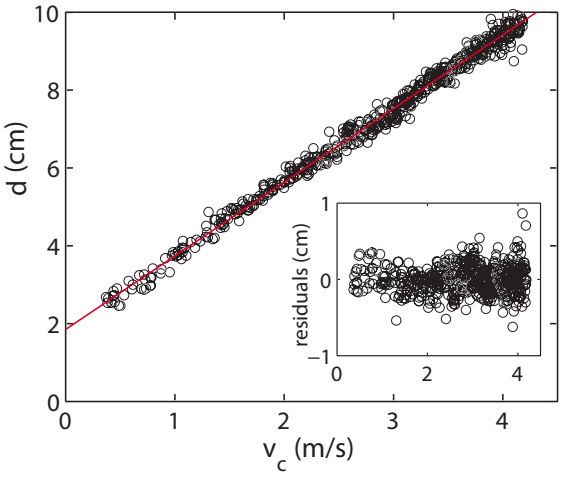

FIG. 2. (Color online) Penetration depth vs impact velocity for a bronze sphere (R=1.91 cm) impacting glass beads. Solid line (red) is a fit to $d=(\Delta d/\Delta v_c)v_c+d_0$ with $\Delta d/\Delta v_c$=0.0189 s and d_0 =0.0185 m. Inset: residuals of the fit.

A. Penetration depth

Previous studies [5,14,15] have discussed the dependence of the penetration depth d on the impact velocity or, equivalently, the total change in potential energy of the impactor (refer to the discussion in the Introduction for scalings obtained in this earlier work). Figure 2 shows that, for large enough v_c, such that a sphere penetrates more than approximately its radius, d increases linearly with v_c. The linear scaling agrees with the data and the scaling proposed in [5]. We do not investigate shallow impact [15] in which this scaling is expected to be modified [14] due to the varying effective cross section of the sphere for $z<R$.

We systematically vary R and ρ_s to determine how the penetration depth changes with these parameters. Since our data indicate that the dependence of d on v_c is close to linear for $d>R$, such that $d=d_0+v_c\Delta d/\Delta v_c$, we compute the slope $\Delta d/\Delta v_c$ and intercept d_0 of d vs v_c and plot these as functions of ρ_s and R as shown in Fig. 3. We compare our results for $\Delta d/\Delta v_c$ vs v_c to the scaling proposed by de Bruyn and Walsh [5], $d\sim(\rho_s/\rho_g)^{1/2}R^{1/2}v_c$, and our results for d_0 vs v_c to the findings of Ambroso *et al.* [15], $d_0\sim(\rho_s/\rho_g)^{3/4}R$, since the former reference makes no predictions for the scaling of d_0. As Figs. 3(a) and 3(b) demonstrate, the slope of d vs v_c scales with the sphere density as $d\sim(\rho_s/\rho_g)^{1/2}$ and with the sphere radius as $d\sim R^{1/2}$ as in [5]. Figures 3(c) and 3(d) indicate that better fits (dashed curves) for the scaling of d_0

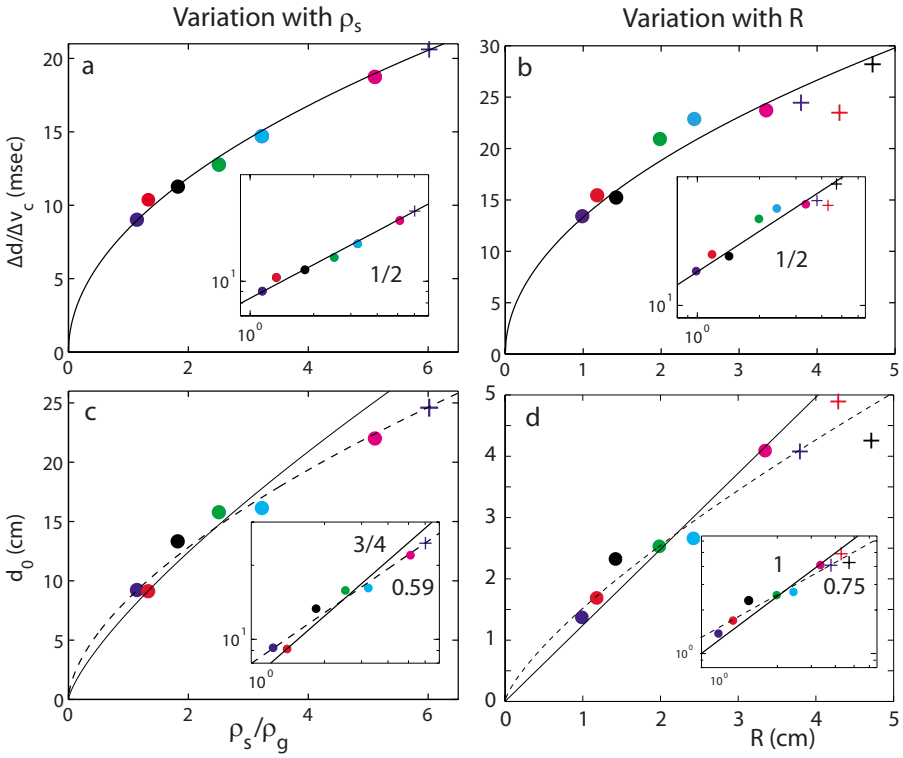

FIG. 3. (Color online) (a),(b) Slope and (c),(d) intercept of linear fits of penetration depth vs sphere impact velocity in glass beads for a 1.9 cm nylon sphere (left column) with ρ_s=1.88, 2.08, 2.85, 3.91, 5.03, 7.97, and 9.38 g/cm^3 (blue, red, black, green, cyan, and magenta ○ and blue +) and steel spheres (right column) with R=0.95, 1.27, 1.51, 1.98, 2.46, 3.49, 3.97, 4.52, and 5.00 cm and corresponding masses m=34.23, 66.3, 112, 287, 531, 1437, 2099, 3055 and 4079 g (blue, red, black, green, cyan, and magenta ○ and blue, red, and black +). The solid curves in (a),(b) are proposed scalings from [5] with $d-d_0 \sim (\rho_s/\rho_g)^{1/2}$ and in (c),(d) from [15] with $d_0 \sim (\rho_s/\rho_g)^{3/4}R$. In (c),(d), the dashed curves are power law fits with exponents 0.59 and 0.75, respectively.

as a function of ρ_s/ρ_g and R are obtained with exponents of 0.59 and 0.75, respectively, as opposed to the predicted values (solid curves) of 0.75 and 1. However, comparison of the measured and predicted values of the exponents is not strictly valid, since our fits apply to the $d>R$ region where $d \propto v_c$, whereas those in [15] are for $d<R$ and give the actual penetration depth of a sphere released at the surface (i.e., $v_c=0$).

Combining these scalings, we write the penetration depth for $d>R$ as

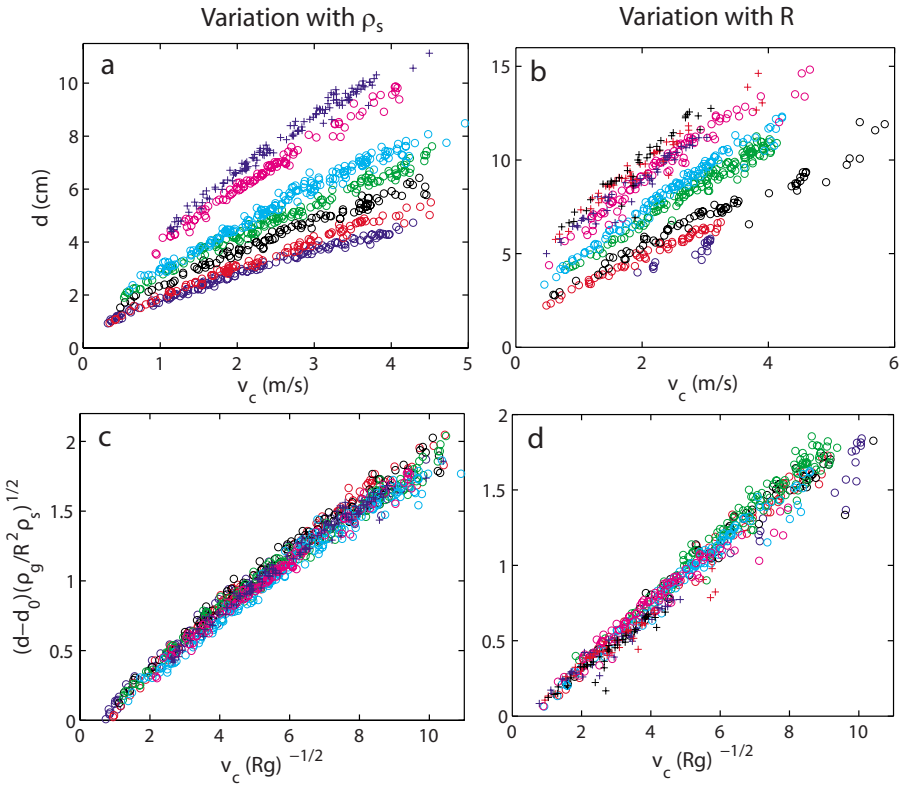

FIG. 4. (Color online) Raw data and collapse using the scalings from Fig. 3. First column (a),(c) Penetration depth and scaled penetration depth vs v_c for varying ρ_s. Second column (b),(d) Penetration depth and scaled penetration depth vs v_c for varying R. Symbols are the same as in Fig. 3.

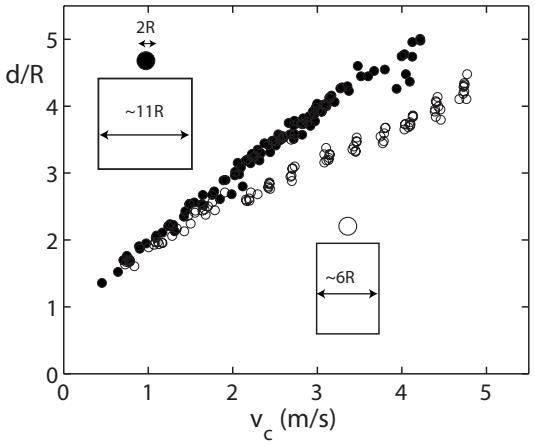

FIG. 5. Container diameter effect on penetration depth. A steel sphere with $R=2.5$ cm impacting glass beads in cylindrical containers with diameters 28 (●) and 14.6 cm (○). Both containers are filled to a depth of approximately 30 cm. The data (●) are reproduced from Fig. 4. The sketches show the relative sphere and container sizes.

$$d = C_1 v_c \sqrt{\frac{R\rho_s}{g\rho_g}} + C_2(\rho_s/\rho_g)^{0.59} R^{0.75}, \tag{4}$$

where C_1 and C_2 are constants. Figure 4 shows both the unscaled penetration depth data and the collapse obtained using Eq. (4). Although we did not systematically investigate the influence of particle (grain) diameter r on penetration depth, Eq. (4) suggests $\Delta d/\Delta v_c \sim r^0$ and $d_0 \sim r^{1/4}$.

Figure 5 shows that the penetration depth is affected by finite container size. Decreasing the container diameter by approximately a factor of 2 decreases the slope of d vs v_c by about 1.3 for $v_c \gtrapprox 2$ m/s. There is little apparent difference in d for smaller v_c. Accordingly, the apparent sublinear dependence of d on v_c evident in the collapsed data in Fig. 4(c) might result from the finite diameter of the container, which, as Fig. 5 indicates, becomes more significant the further the impactor penetrates.

B. Collision duration t_c

1. Lack of dependence of t_c on v_c

In a previous quasi-2D study of disks impacting smaller disks confined between narrow sidewalls, Ciamarra *et al.* found that the collision duration t_c was independent of v_c [4]. They attributed this to a constant acceleration during impact whose magnitude was linearly dependent on v_c. Our acceleration data for a 3D disk reveal that t_c (defined here as the time from impact to arrest; see, e.g., Fig. 1) is nearly independent of v_c for $v_c \gtrsim 1.5$ m/s (see Fig. 6). We denote this velocity-independent collision duration as t_0. Unlike in [4], but as is the case for spheres, we find that the acceleration is not constant during the penetration phase (see inset of Fig. 6); we return to analysis of the acceleration in Sec. IV. Below $v_c \approx 1.5$ m/s, t_c decreases and as $v_c \to 0$, $t_c \to 0$. This decrease at low velocity is a consequence of the finite yield stress of granular materials (incorporated in the model of de Bruyn and Walsh [5]), which allows support of a distributed finite load without penetration [21].

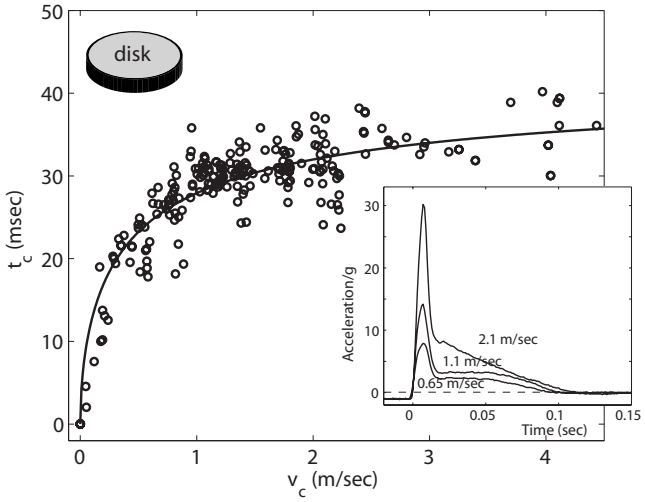

FIG. 6. Collision duration for impact of an $R=1.0$ cm, $m=0.01$ kg disk with glass beads. Solid line shows fit from the model [14] proposed for large impact velocity (deep penetration) with $\alpha=1.45$ kg/m and $F_z=0.233$ N. At low velocity t_c increases with v_c which is the opposite of the behavior for spheres (see Figs. 7 and 9).

We now make an argument for the dependence of t_c on v_c for disk impact based on the model of [14] in the deep collision regime. Using Eqs. (1) and (2) with constant F_z, appropriate for the regime of deep impact velocity [14], we write

$$dt = \frac{dv}{(F_z/m - g) + \frac{\alpha}{m}v^2}. \tag{5}$$

We supplement this equation with the boundary condition for a disk such that $v(t=0) = -v_c$. Integration yields $t = \frac{\tan^{-1}[v\sqrt{\alpha/(F_z - mg)}]}{\sqrt{\alpha(F_z/m^2 - g/m)}} + C_1$ with $C_1 = \frac{\tan^{-1}[v_c\sqrt{\alpha/(F_z - mg)}]}{\sqrt{\alpha(F_z/m^2 - g/m)}}$.

We define the collision time t_c as the interval between initial contact and the moment the disk comes to rest (i.e., $v=0$):

$$t_c = \frac{\tan^{-1}[v_c\sqrt{\alpha/(F_z - mg)}]}{\sqrt{\alpha(F_z/m^2 - g/m)}}. \tag{6}$$

This solution is plotted in Fig. 6 and is a good fit to the experimental data; α and F_z are fit parameters. As $v_c \to \infty$ for nonzero $\sqrt{\alpha/(F_z - mg)}$, t_c approaches $t_0 = \pi/2\sqrt{\frac{m}{\alpha(F_z/m - g)}}$, a constant independent of v_c.

The asymptotic form of t_c given above allows a prediction of scaling behavior of t_0 with experimental parameters. Using $F_z \sim \rho_g g R^3$ and $\alpha \sim \rho_g R^2$ as predicted in [6,14], t_0 should scale as

$$t_0 \sim \left(\frac{\rho_s}{\rho_g}\right)\sqrt{R/g}. \tag{7}$$

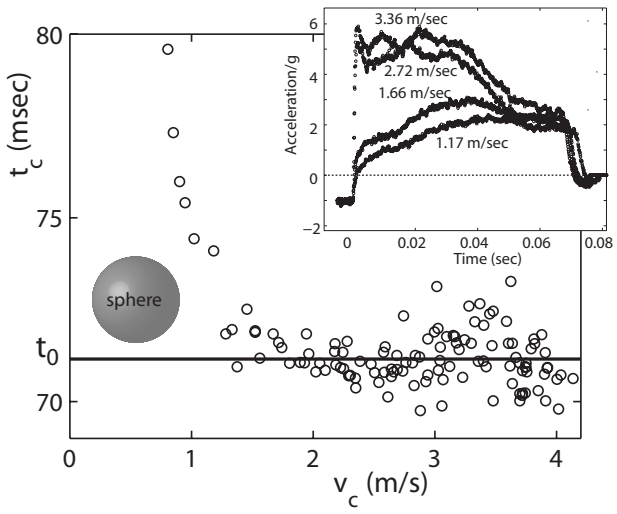

FIG. 7. Collision time t_c is independent of collision velocity v_c for sufficiently high v_c ($R=2.0$ cm steel sphere into glass beads). Inset: acceleration vs time for four impact events showing that, while t_c is independent of v_c, the acceleration profile is not.

This equation is expected to depend on impactor and grain geometry, density, friction coefficients, normal dissipation, and other material parameters.

2. Scaling of t_0 in sphere data

The experimental result for the disk data showing that $t_c \to t_0$ as v_c increases is also seen in our sphere data (see Fig. 7). Similarly, the acceleration during collision is not constant (see inset of Fig. 7). The large range of system parameters considered in the sphere data set allows us to examine how t_0 scales with radius, density, and gravitational acceleration.

In contrast to the disk, in which $t_c \to 0$ as $v_c \to 0$, t_c *increases* with decreasing impact velocity for spheres; compare Figs. 6 and 7 for $v_c \lessapprox 1.5$ m/s. We attribute this difference to the fact that, even as $v_c \to 0$, the small initial contact area between sphere and grains due to the curvature of the sphere always produces local stresses sufficient for grain bed yielding, which consequently allows the sphere to penetrate for a finite time. Thus, a sphere, unlike a disk, always penetrates a finite distance into the material even with $v_c=0$; this penetration regime has been examined in [5,16].

For sufficiently high v_c, the surface of the sphere in contact with the granular medium is expected to be essentially constant for a large fraction of the collision interval after the initial impact [14]. We therefore expect the proposed scaling of Eq. (7) for disks to be obeyed for spheres as well in the high-v_c regime. As shown in Fig. 8, we find that $t_0 \sim R^{1/2}$ and $t_0 \sim (g_{\text{eff}})^{-1/2}$, where g_{eff} is the acceleration of the falling bucket in the Atwood machine. For impact at varying sphere densities, the figure shows that $t_0 \sim (\rho_s/\rho_g)^{1/4}$.

Combining these three scalings, we obtain

$$t_0 \sim \left(\frac{\rho_s}{\rho_g}\right)^{1/4} \sqrt{R/g}, \tag{8}$$

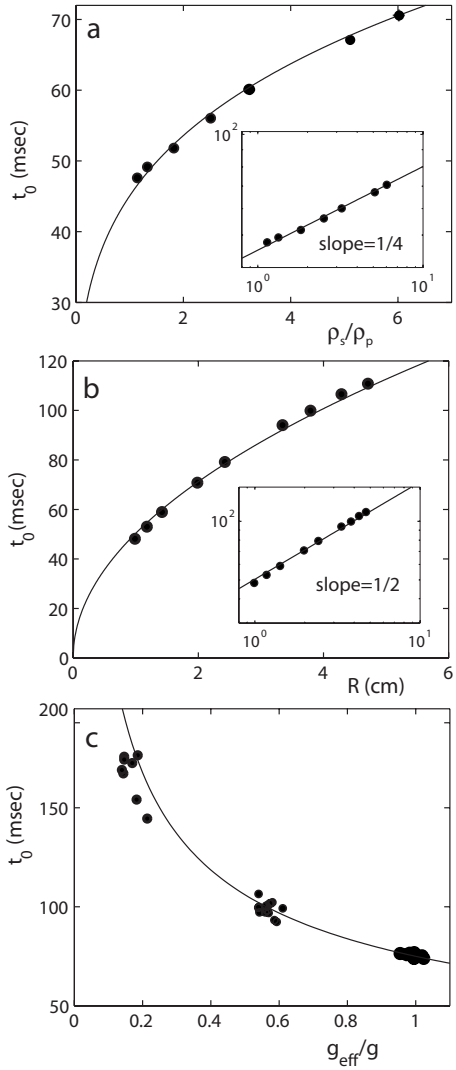

FIG. 8. Scaling of asymptotic ($v_c > 1.5$ m/s) penetration time t_0 for impact into glass beads as a function of (a) sphere density for the $R=1.9$ cm nylon sphere [fit shown with t_0 in seconds is $t_0 = 0.045(\rho_s/\rho_g)^{1/4}$], (b) sphere radius for steel spheres (fit shown is $t_0 = 0.050R^{1/2}$), and (c) effective gravitational acceleration for an $R = 1.98$ cm steel sphere [fit shown is $t_0 = 0.075(g_{\text{eff}}/g)^{-1/2}$].

or in terms of the sphere mass $t_0 \sim [M/(Rg^2\rho_g)]^{1/4}$. A test of this final scaling is shown in Fig. 9 which shows that the t_c data collapse well for a large range of densities and radii. Comparison of the experimentally determined t_0 scaling with our model shows that Eqs. (8) and (7) both include a $\sqrt{R/g}$ term but have different exponents in the density term (1/4 and 1, respectively). If these equations are equivalent, the latter result implies that C in Eq. (7) should vary as $(\rho_s/\rho_g)^{-3/4}$.

IV. DYNAMICAL FEATURES OF IMPACT

While t_c and d are characteristic physical quantities associated with any impact into deformable material, we hypothesize that the scaling that matches experimental data can be obtained with a variety of phenomenological models

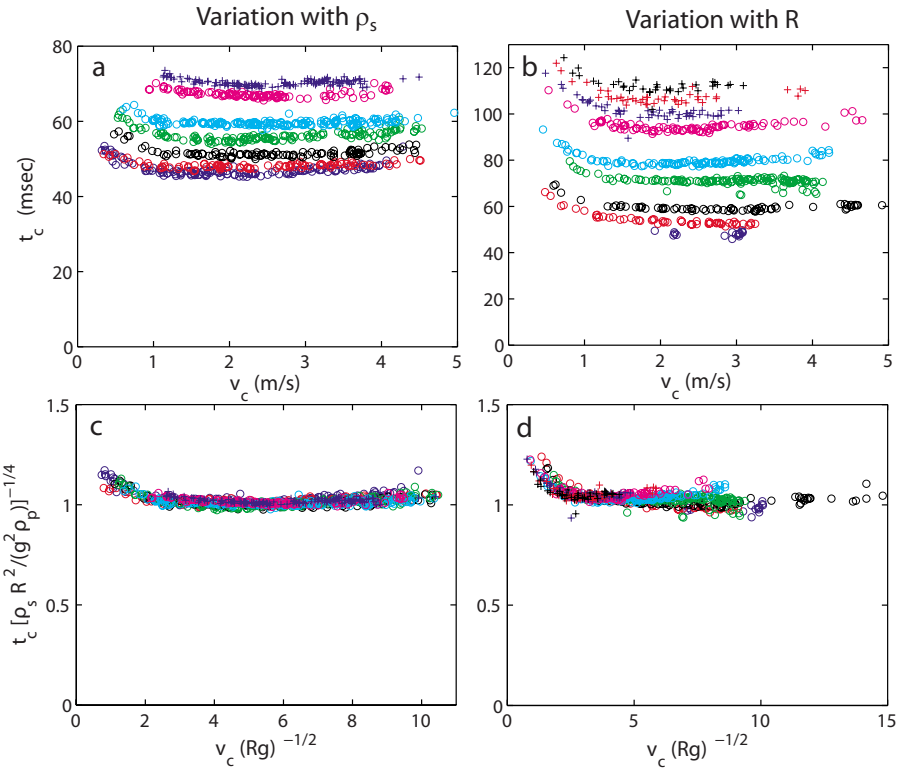

FIG. 9. (Color online) Test of scaling derived from data in Fig. 8. Collision time vs v_c for (a),(c) varying sphere density (nylon sphere with added masses) and (b),(d) varying sphere radius (steel spheres). The data in (c),(d) are rescaled data using Eq. (8). The effective densities of the $R=1.91$ cm nylon sphere are $\rho_s=1.88$, 2.08, 2.85, 3.91, 5.03, 7.97, and 9.38 g/cm^3, corresponding to blue, red, black, green, cyan, and magenta ○ and blue +. The radii of the steel spheres are $R=0.95$, 1.27, 1.51, 1.98, 2.46, 3.49, 3.97, 4.52, and 5.00 cm with associated masses ranging from $m=34$ to 4079 g (blue, red, black, green, cyan, and magenta ○ and blue, red, and black +).

(see references in Sec. I). In contrast, examine Fig. 10, which shows the acceleration profiles for impact of an $R=1.91$ cm diameter nylon sphere for five distinct impact velocities. As this figure makes clear, while current models capture the average physics involved in the impact events, they miss much of the detailed physics involved in a collision. As an example, we fit the data in Fig. 10 to the model of Ambroso *et al.* [15]. As v_c increases, the model fails to capture significant acceleration fluctuations as well as the underlying form of the acceleration. Figure 11 shows the corresponding growth in the relative error between experimental data and the model fit as v_c increases.

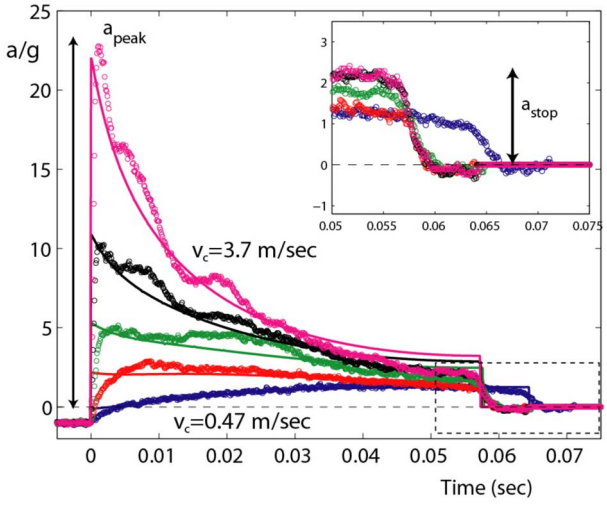

FIG. 10. (Color online) Acceleration profiles for different impact velocities (v_c=0.47, 0.93, 1.99, 2.88, and 3.72 m/s, blue, red, green, black, and pink) for a 147 g nylon sphere (R=1.9 cm) impacting polydisperse 0.25–0.42 mm glass beads. Dynamical features shown and discussed in the text are the peak acceleration a_{peak}, the jump in acceleration as the sphere comes to rest, a_{stop} (see inset), and the time for the object to come to rest, t_c. The open symbols are experimental data; the solid lines are best fits using the model of Ambroso *et al.* [15]; parameters of the fit are given in the text and in Fig. 12. Fits are not shown in the inset.

The force model from [15] has a second shortcoming: It predicts that the scaling lengths d_0 and d_1 in Eq. (3) are independent of v_c. Least-squares fits of $a(t)$ for fixed sphere

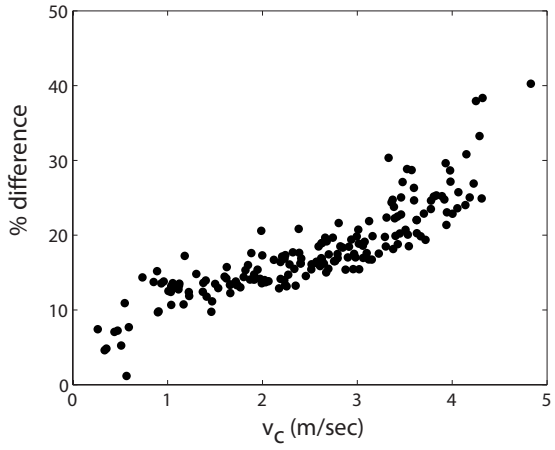

FIG. 11. Increasing deviation in average percentage difference between experimental data and best fits to the model of [15] [see Eq. (3)] from the data set used in Fig. 10. The percentage difference calculation is averaged over the central 70% of the data and model fit.

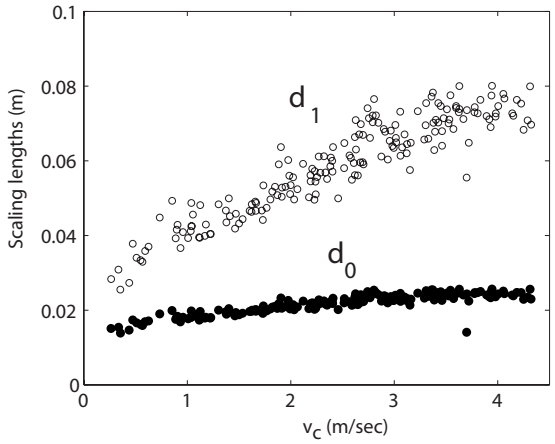

FIG. 12. Scaling lengths d_0 (●) and d_1 (○) in the model of [15] [see Eq. (3)] as determined by best fits to the data set from Fig. 10 are not constants as predicted by the model but depend on the impact velocity.

mass M while d_0 and d_1 are allowed to vary are shown for different v_c in Fig. 10. The dependence of d_0 and d_1 on v_c is shown in Fig. 12. Although d_0 is roughly independent of v_c, d_1 increases with increasing v_c. Since the model fails to account for the dependence of d_0 and d_1 on v_c, this indicates that additional physics is needed to fully characterize impact dynamics.

Therefore, we now discuss the detailed acceleration profile of a sphere as it impacts a granular medium. We first describe two robust acceleration features seen for a wide range of impactor radii, densities, and material types, as well as for a range of granular materials: A peak in the acceleration during collision, a_{peak}, and a rapid decrease in the acceleration as the object comes to rest, a_{stop}; see Fig. 10. For impact at fixed parameters (i.e., v_c, R, ρ_g, and ρ_s) Fig. 13 shows that the acceleration profile and associated features are reproducible to within approximately 5% from run to run. We demonstrate how these dynamical features scale with system parameters. Using insights gained from the scaling,

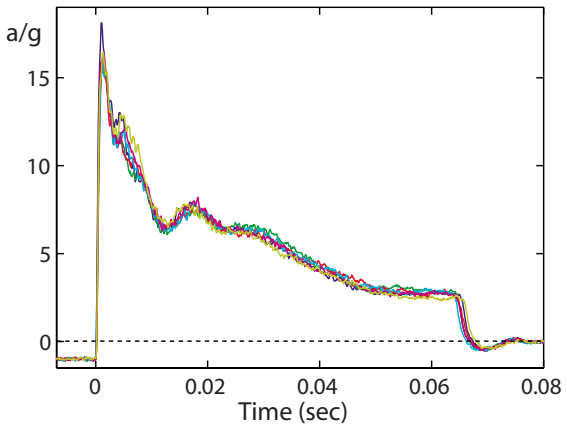

FIG. 13. (Color online) Details of the acceleration profiles show only small variation (net $<5\%$) from run to run for six separate impacts of an $R=1.91$ cm bronze sphere into glass with initial velocity $3.65<v_c<3.67$ m/s.

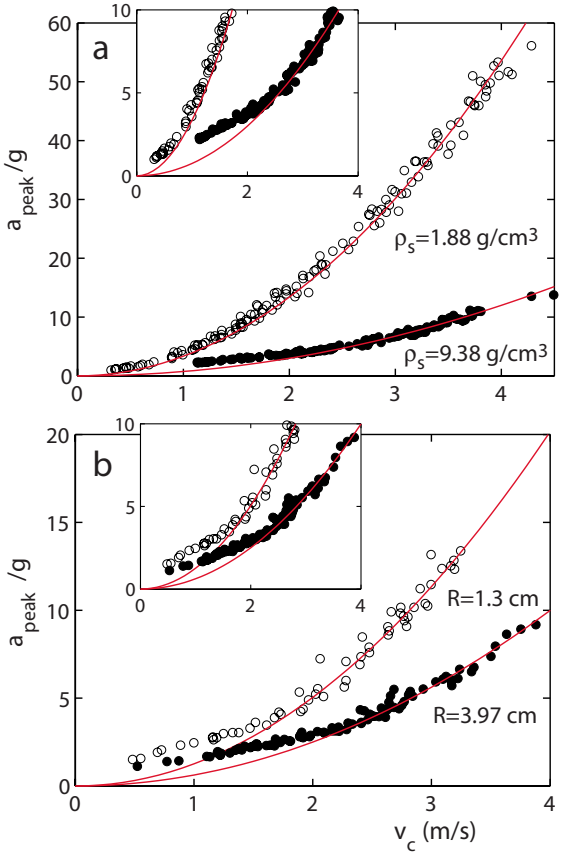

FIG. 14. (Color online) Peak impact acceleration a_{peak} as a function of impact velocity into glass beads for (a) a nylon sphere with effective density 1.88 and 9.38 g/cm^3 and $R=1.9$ cm, and (b) steel spheres with radii $R=1.3$ and 3.97 cm. Solid lines are fits of $a_{\text{peak}} \sim v^2$ for $v_c \gtrapprox 1.5$ m/s. The inset shows that, as $v_c \to 0$, the v_i^2 scaling does not hold.

we deduce an empirical force model by examining the experimental data in the extremes of high velocity with shallow penetration and low velocity with deep penetration.

A. Peak accelerations

During the collision the acceleration rises to a maximum whose magnitude we denote a_{peak}. At low velocity, the peak is not pronounced, but rather is seen as a broad maximum. As v_c increases, the peak occurs soon after the initial contact of the sphere with the grain surface. For $v_c \gtrapprox 1.5$ m/s the interval between contact and peak acceleration is only a few milliseconds. Figure 14 shows that in this regime, for all sphere densities and radii, a_{peak} increases approximately as v_c^2. $a_{\text{peak}} \sim v^2$ is in accord with all models [6,14,15] in the high-velocity and low-depth limits, and implies that for these v_c the impact fluidizes grains sufficiently for the system to display inertial fluidlike drag [22]. For fixed v_c, a_{peak} can increase by more than 50% if the container is sharply tapped a few times before impact. But, as Fig. 13 indicates, preparation by rocking produces consistent results.

At low impact velocity as $v_c \to 0$, a_{peak} does not approach zero, but instead approaches a finite intercept; see the insets

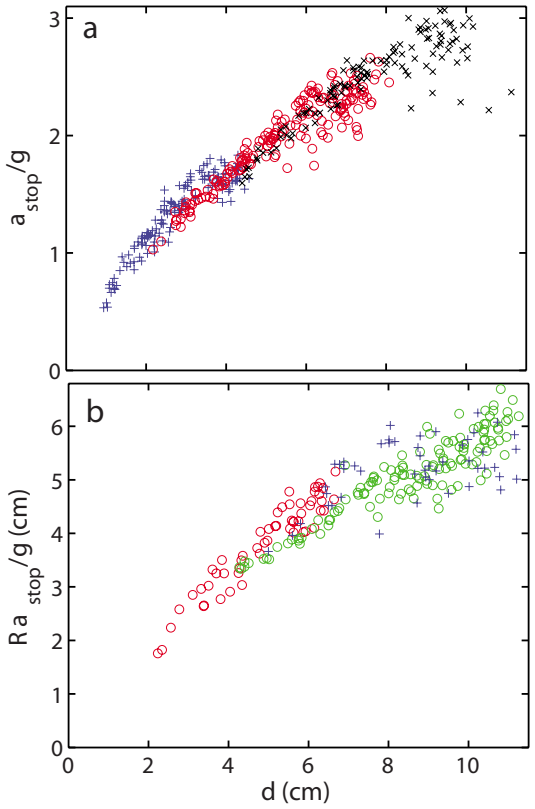

FIG. 15. (Color online) (a) Scaling of a_{stop} vs impact depth for an $R=1.91$ cm nylon sphere with effective densities $\rho_s=1.78$, 5.03, and 9.39 g/cm^3 (blue +, red ○, and black ×) and corresponding masses $m=51.6$, 146, and 272 g. (b) a_{stop} scaled by sphere radius vs impact depth for steel spheres of radii $R=1.3$, 2.0, and 4.0 cm with masses $m=83.3$, 287, and 2099 g (red and green ○ and blue +).

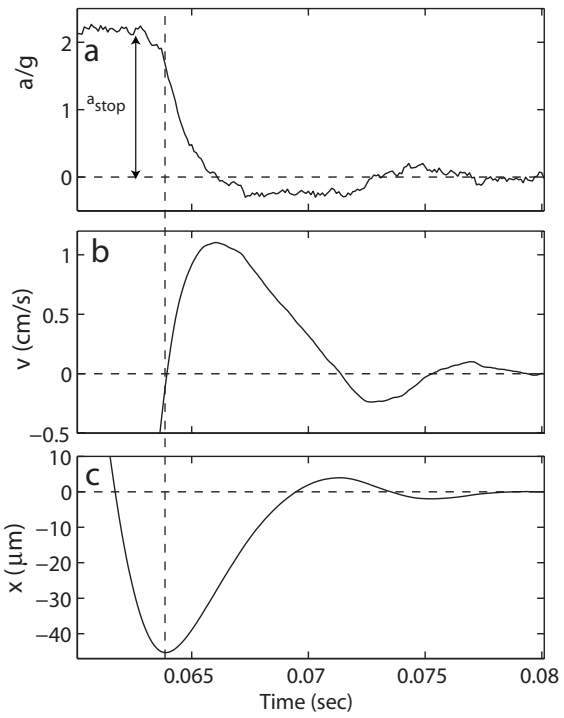

FIG. 16. The end of the collision ($a<a_{stop}$) displays (a) overshoot in acceleration which leads to (b) reversal of the collision velocity and (c) rebound in position for an $R=1.91$ cm bronze sphere colliding with glass beads at $v_c=2.4$ m/s. (Time axis is zero at start of collision.)

of Fig. 14. Figure 10 shows that in the low-velocity limit the peak acceleration occurs at the end of the collision just before the sphere comes to rest. We interpret this as a change from hydrodynamiclike dynamics at high velocities to a regime in which resistance to inertia is no longer the dominant source of drag. This is consistent with Fig. 14(a) which shows the lower-density sphere scaling as v_c^2 over a larger velocity range than the higher-density sphere; the latter's velocity decreases more slowly, resulting in deeper penetration where the influence of $F(z)$ is no longer negligible. Since high- and low-velocity regimes are dominated by different physics, we postpone further discussion of a_{peak} until the treatment of force laws in Sec. IV C.

B. Stopping acceleration

For all v_c, the sphere does not come to rest gradually, but instead suffers an abrupt decrease in acceleration before halting, which is reminiscent of a horizontally sliding object stopping due to friction. We denote the magnitude of the decrease as a_{stop}. This impact feature occurs for all spheres, granular materials, and containers we employed in our study. As can be seen in the inset of Fig. 10, a_{stop} increases with increasing v_c. The models of both Tsimring and Volfson [14] and Ambroso *et al.* [15] predict jumps in the acceleration as the impactor comes to rest, which are attributed to the dominance of the depth-dependent frictional or hydrostatic drag term F_z. While the models predict that $a(t)$ instantaneously jumps to zero at the end of penetration, we observe that the rate at which $a(t)$ decreases to zero depends on v_c; as v_c increases, the transition to $v=0$ sharpens (see inset of Fig. 10). We comment on this in Sec. IV C.

In Fig. 15 we examine a_{stop} as a function of penetration depth d for varying sphere density ρ_s and radius R, where d is the depth to which the lowest point of the sphere penetrates the material (see Sec. III A). For varying ρ_s [Fig. 15(a)] and constant R, we find that a_{stop} is *independent* of the sphere density—at the same depth spheres of different density experience the same jump in acceleration (i.e., force is proportional to mass), further evidence for frictional forces dependent primarily on geometry dominating the final stages of penetration. a_{stop} increases as the ultimate penetration depth of the sphere increases. For $d\gtrsim 2$ cm, a_{stop} increases approximately linearly, although there is increased scatter toward lower a_{stop} for $d\gtrsim 7$ cm. For $d\lesssim 2$ cm, a_{stop} increases more rapidly with increasing d. We attribute this larger slope at small d to the initial growth in contact area between sphere and grains that occurs as the sphere submerges.

For spheres with varying radii and constant density, a_{stop} also increases with depth, again with increased scatter for larger d. Unlike its density independence, a_{stop} is inversely proportional to sphere diameter at any given depth. Figure 15(b) shows that, when Ra_{stop} is plotted vs d, data sets for spheres of various radii fall onto the same curve. This col-

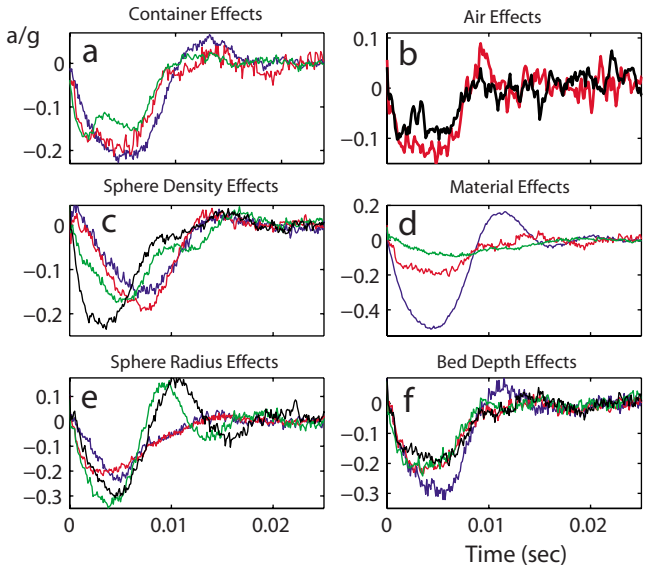

FIG. 17. (Color online) Dependence of the final stage of the collision (see Fig. 16) on system parameters. (a) Collisions averaged over interval with $2<v_c<5$ m/s in a cardboard barrel (blue), a PVC bucket (red), or an aluminum pot (green) (see text for container details). (b) $R=2.0$ cm steel sphere with $v_c=1.35$ m/s dropped into a 7-cm-deep bed at atmospheric pressure (black) and at 50 mTorr (red). Data are an average of six collisions for each pressure. (c) $R=1.9$ cm nylon sphere with $\rho_s=1.88$, 2.85, 5.03, and 9.38 g/cm^3 (blue, red, green, and black). Data are an average over collisions with $2<v_c<5$ m/s. (d) Collision with bird seed, glass beads, and cut aluminum wire in aluminum pot (blue, red, and green). (e) Steel spheres $R=1.3$, 2.0, 3.5, and 4.5 cm (blue, red, green, and black). (f) Layer depths of 8, 10, 15, and 20 cm (blue, red, green, and black). Glass beads are the granular medium in (a)–(c), (e), and (f), an $R=1.9$ cm bronze sphere is the impactor in (a) and (d)–(f), and the plastic bucket holds the grains in (c), (e), and (f).

lapse holds for our entire steel sphere data set in which m varies by more than two orders of magnitude (for clarity, the full data set is not shown). When multiplied by R the a_{stop} data for varying density also fall onto the same curve.

In the final stage of the collision in the vicinity of a_{stop}, the sphere responds as if it were in contact with an elasticlike medium (see Fig. 16). The sphere does not instantaneously come to rest at $v=0$ as predicted by models, but instead the acceleration decreases rapidly (with finite slope) and overshoots (negative acceleration). When the rapid decrease in $a(t)$ associated with a_{stop} begins, the velocity increases through zero, indicating that the sphere has reached it deepest penetration, reversed direction, and is moving upward; for some impact parameters [see Figs. 17(d) and 17(e)], the velocity and position oscillate for a few cycles after the initial overshoot. Recently Durian and co-workers [18] also observed an oscillation in the velocity of a sphere at the end of the collision. They attributed this to displacement of the bottom of the container, but for our data, as seen in Fig. 17(a), the primary overshoot is largely independent of container size and composition for three different containers: cardboard (blue), PVC (red), and aluminum (green) (see Table III for container details). Nor does the interstitial air diminish the effect, as Fig. 17(b) shows for glass beads. Other evidence pointing to an intrinsic origin is provided by Fig. 17(c), which shows that as the sphere density increases at fixed R the duration of the overshoot *decreases,* and by Fig. 17(d), which shows that with the same impactor and container the overshoot varies with the granular material. Additionally, the overshoot is observed to decrease with increasing sphere radius [see Fig. 17(e)] but to be largely independent of bed depth for depths ranging from 8 to 20 cm. We speculate that, when the acceleration reaches a_{stop}, the material suddenly undergoes a solidification transition and the subsequent dynamics are a result of the sphere oscillating within the now elastic solid as Fig. 16(c) suggests and as modeled by [5]. This picture does not explain why the characteristic overshoot time decreases with increasing sphere density.

C. Discussion of force laws

The preceding results for a_{peak} and a_{stop} suggest that hydrodynamic forces scaling like v^2 dominate in the high-velocity and shallow-penetration regime, while frictional and

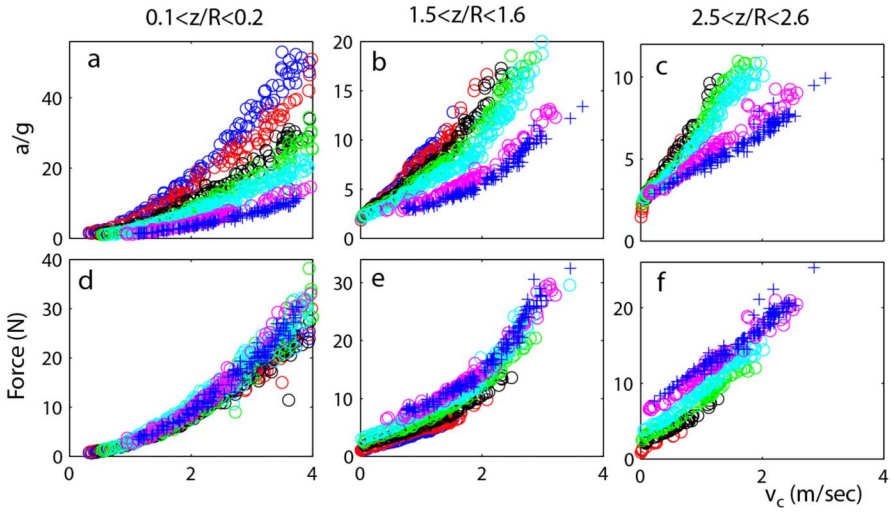

FIG. 18. (Color online) Acceleration ([top panels (a)–(c)] and force $m(a-g)$ [bottom panels (d)–(f)] of an $R=1.91$ cm nylon sphere with different effective densities vs velocity at three distinct scaled depths z/R during impact. Depths are written above each column and correspond to (a),(d) initial impact, (b),(e) penetration of $\approx$1.5 sphere radii, and (c),(f) penetration of $\approx$2.5 sphere radii. Sphere densities $\rho_s=1.88$, 2.08, 2.85, 3.91, 5.03, 7.97, and 9.38 g/cm^3 correspond to blue, red, black, green, cyan, and magenta ○ and blue +.

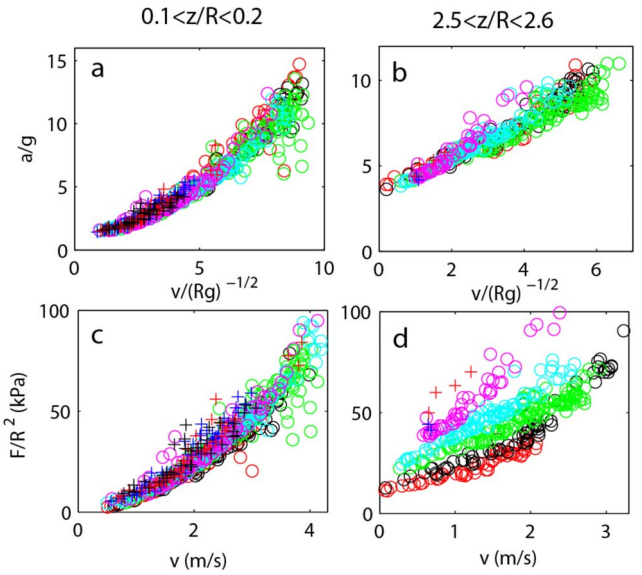

FIG. 19. (Color online) Acceleration [top panels (a),(b)] and force $m(a-g)$ [bottom panels (c),(d)] of steel spheres of different radii at three scaled depths z/R during impact. Depths are written above each column and correspond to (a),(b) initial impact and (c),(d) penetration of ≈ 2.5 radii. Sphere radii are $R=0.95$, 1.27, 1.51, 1.98, 2.46, 3.49, 3.97, 4.52, and 5.00 cm with corresponding masses $m=34.23$, 66.3, 112, 287, 531, 1437, 2099, 3055, and 4079 g (blue, red, black, green, cyan, and magenta ○ and blue, red, and black +).

hydrostatic forces are of primary importance as $v \to 0$. To examine these ideas, Figs. 18 and 19 show the velocity dependence of sphere dynamics at various fixed depths during the collision. For shallow depths and varying densities, the accelerations are different but the forces exerted by the grains, $F=m(a-g)$, collapse onto a master curve such that $F \sim v^2$ [see Figs. 18(a) and 18(d)]. Thus, as assumed by [6,7,10,13–15], a drag force proportional to the velocity squared, and independent of mass, is a good approximation for shallow depths. Additionally, [6,7,10,13–15] assume the force is inversely related to the sphere cross-sectional area. To check this scaling we plot in Figs. 19(a) and 19(c) a/g vs $v/\sqrt{Rg}$ and F/R^2 vs v at shallow depth and for varying radii. Both quantities fall onto master curves varying as v^2, indicating that indeed $F \propto R^2$.

For deeper penetration and decreasing velocity, the force and acceleration no longer vary as v^2, but are instead linear in velocity with a nonzero offset at $v=0$; see Figs. 18(c), 18(f), 19(b), and 19(d). The slope of F vs v is independent of mass [see Fig. 18(f)], suggesting a low-Reynolds-number fluidlike drag. However, as indicated by Figs. 19(b) and 19(d), the linear velocity coefficient of the force varies as $R^{5/2}$ rather than R as is the case for Newtonian fluids. Linear velocity dependence has been proposed in [5,6,13], although v_c was much larger ($v_c \sim 700$ m/s in [6,13]) than in our study. For both varying density and varying radii, the extrapolated $v=0$ intercept occurs at constant acceleration, indicating a force dominated by friction. We note that at very low velocities ($v \lesssim 0.25$ m/s) a becomes constant—this is

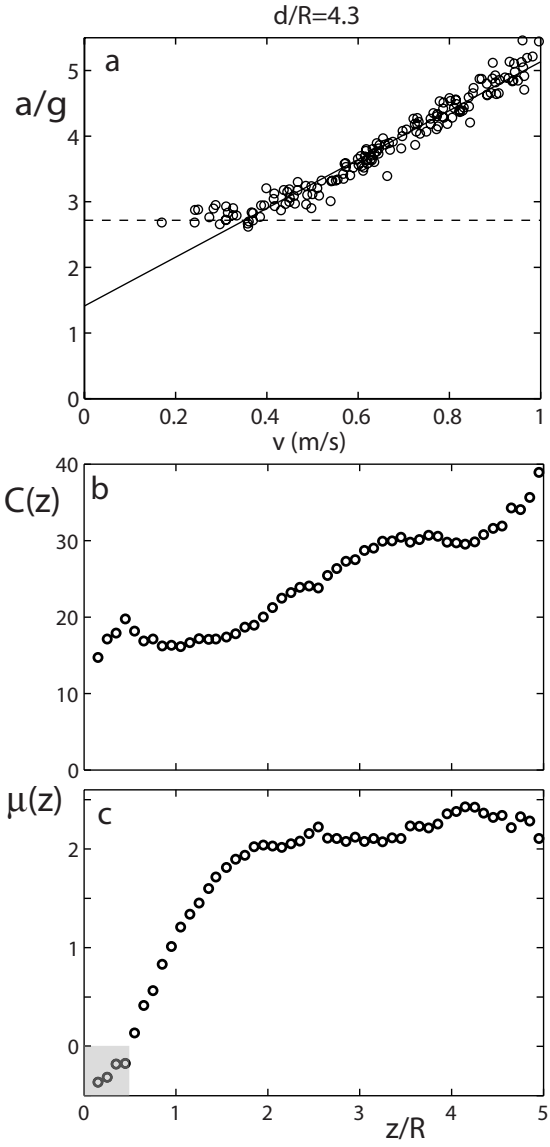

FIG. 20. (a) Acceleration of an $R=1.9$ cm bronze sphere vs velocity in the final stages of collision with glass beads (fixed depth $z/R=4.3$). The dashed line shows how a_{stop} is determined and the solid line shows the linear fit region for this fixed depth. Compare to Figs. 18(c) and 18(b). (b),(c) Coefficients in Eq. (9) vs penetration depth for impact of an $R=1.9$ cm bronze sphere into glass beads obtained from such fits. The fit region (see Fig. 18) is for $0.25 < v < 1.25$ m/s. The $\mu < 0$ region (shaded) in (c) is a result of applying a linear fit when the v^2 term is dominant.

the regime of a_{stop} [see Fig. 20(a) for example] and explains why $a_{\text{stop}} \geqq \mu g$.

Summarizing the results of Figs. 18 and 19, we write the drag force F_d exerted by the granular medium on the sphere as the empirical force law

$$F_d = \mu(z)mg + C(z)R^{5/2}\rho_g\sqrt{g}v + \alpha' R^2 v^2, \qquad (9)$$

where $\mu(z)$ is a depth-dependent constant analogous to a friction, $C(z)$ is a drag coefficient also dependent on depth, and α' is a constant independent of depth. We consider this

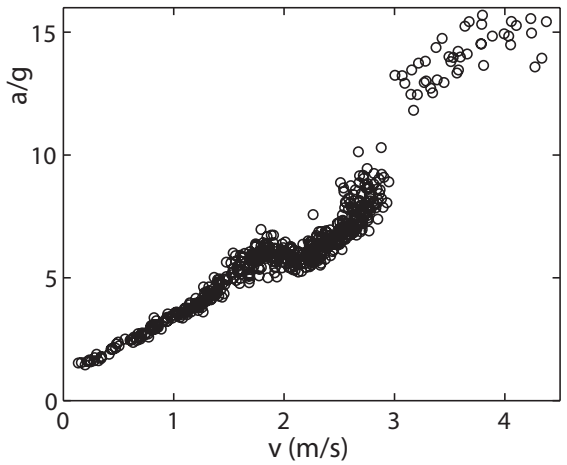

FIG. 21. Acceleration of an $R=1.9$ cm bronze sphere vs velocity at intermediate stages of collision with glass beads (fixed depth $1.85<z/R<1.91$) shows nonmonotonic behavior (compare to Figs. 14 and 15).

equation to be valid in the "steady" collision regime before the sidewalls of the crater start to collapse onto the impacting sphere (i.e., before the sudden jump in a at a_{stop} and the subsequent upward motion of the sphere). The variation of μ and C with depth is shown in Fig. 20. The saturation of $\mu(z)$ with penetration depth in the velocity-independent term in Eq. (9) is in accord with the models of [14,15]. However, as we mention in our discussion of a_{stop}, this saturation appears to be associated with a constant effective contact area between the sphere and grains rather than a hydrostatic pressure since μ is independent of mass [e.g., see Figs. 18(c) and 19(b)]. In Eq. (9) the linear velocity term follows the model in [5] for the scaling of F_d with R and g. However, we find that our force law is independent of ρ_s but proportional to ρ_g, while [5] reports that the drag force scales as $\sqrt{\rho_s \rho_g}$.

Finally, despite its agreement with our data in both the high-velocity and shallow-penetration and low-velocity and deep-penetration regimes, the empirical model for sphere impact proposed in Eq. (9) is incomplete: the force in the intermediate stages of collision exhibits a more complicated and nonmonotonic dependence on $v(t)$ as seen in Fig. 21. This nonmonotonic behavior may be the result of local changes in the grain layer caused by wave propagation in the bulk. Nor have we examined how μ, C, and α vary with the grain-grain and grain-intruder friction coefficients. For example, preliminary experiments show that, for collision with glass beads, t_c is reduced by approximately 5% when a monolayer of glass beads is glued to the nylon sphere. Modifications to Eq. (9) will also be required to describe collisions of constant-cross-section intruders (e.g., see the disk data in Sec. III B) and other nonspherical objects.

D. Fluctuations and material dependence

For sufficiently low impact velocity, the model of [15] captures the shape of the acceleration profile (see Figs. 10 and 11). As v_c increases, the relative difference between the experimental data and the model prediction increases. For low velocity, the acceleration is concave down. According to the model, the force on the sphere increases as the sphere penetrates into the medium, and then smoothly levels out to a constant. As v_c increases, the curves develop upward concavity. Substantial fluctuations in our experiments appear in the vicinity of the change in curvature, which implies that they are associated with penetration dynamics dominated by the inertial v^2 term. The models discussed in this paper cannot capture such physics as they are purely hydrodynamic. In addition, Fig. 22 demonstrates that the fluctuations depend on the type of material that the sphere impacts. The fluctua-

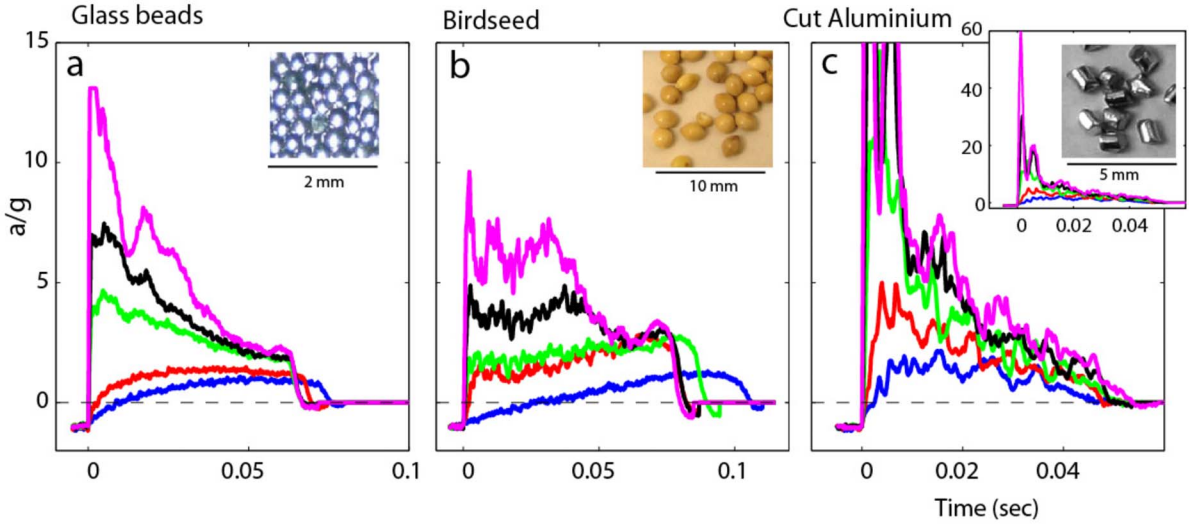

FIG. 22. (Color online) Fluctuations in acceleration during penetration depend on the characteristics of the material being penetrated. An $R=1.9$ cm, $m=200$ g bronze sphere impacting (a) glass spheres, (b) birdseed, and (c) cut aluminum wire (see Table I for material properties). Impact velocities (blue, red, green, black, and magenta) are $v_c=$ (a) 0.45, 0.84, 1.82, 2.47, and 3.40, (b) 0.5, 1.22, 1.74, 2.51, and 3.53, and (c) 0.50, 0.98, 1.79, 2.43, and 3.36 m/s.

tions are significantly more irregular and occur over shorter time scales in millet seeds (smallest density) and aluminum (largest density) than in glass beads, which exhibit a characteristic structure for higher v_c (see also Fig. 21). We attribute the fluctuations in acceleration to creation and annihilation of elements of the force network [23]. These fluctuations are apparently strongly influenced by particle shape and also size relative to the impactor. They have mostly been observed in the quasistatic regime [24] although quantitative study using photoelastic particles is possible [25].

As Fig. 22 also shows, a_{peak} increases with the particle density ρ_g such that the densest material (aluminum) has a peak acceleration approximately six times that of the millet seeds (birdseed) at a given v_c; the density ratio of the particles is approximately a factor of 2 (see Table I). However, the magnitude of a_{stop} and the overshoot at the end of the collision are largest for the millet seed and smallest for aluminum, which is opposite to the behavior of a_{peak}. The collision time t_c decreases monotonically with increasing particle density.

V. CONCLUSIONS

We have directly measured the forces experienced by spheres and disks impacting granular media at collision velocities $v_c < 5$ m/s. By integrating the measured acceleration we have deduced scaling relations for penetration depth and collision time as a function of v_c and collision impactor parameters and compared them to scalings proposed in the literature. We have identified robust features of the collision dynamics (a_{peak} and a_{stop}) and described how they scale with v_c and intruder parameters. These features are in accord with models of drag that propose both inertial and frictional drag terms. We have shown how the combination of such terms determines the surprising finding that the time of collision is independent of velocity. Developing the force law for penetration empirically from our data, we have proposed a model of the drag force on a sphere during impact which includes constant, linear, and quadratic terms, and have shown how the coefficients in this drag relation scale with v_c and intruder parameters. We have discovered that during impact significant fluctuations in acceleration occur which are not described by any existing models of impact. Whether these material-dependent fluctuations fall outside the scope of continuum dynamics remains to be determined.

The solid volume fraction ϕ was not varied in our experiments. However, previous work on penetration of granular media at constant low velocity [26] revealed a ϕ-dependent transition in penetration force apparently associated with the onset of glassy behavior [27]. Future studies should investigate whether impact dynamics exhibit a similar ϕ dependence.

Our experiments provide another example of the rich dynamics and fundamental physics found in the interaction of objects with granular media in the mixed fluid-solid regime. While there has been much progress in the theory of free granular flow (hydrodynamic regime) [28–31], models describing the mixed regime examined here are not rooted in fundamental physics but are largely phenomenological. Our data can constrain and inform development of models in this regime. We hypothesize that, to accurately capture the dynamics we have observed (including fluctuations and stopping acceleration), the physics of rapid fluidization and solidification must be included. Beyond discrete simulations [4], multiphase modeling like that proposed in [32] might be applicable, or perhaps such features will have to be captured by statistical models.

In addition to probing challenging and unsolved problems in the physics of granular media, models describing the impact regime we have studied here are important to many areas of science and engineering. One area with increasing relevance is control of locomotion in organisms and robots [33,34]. Movement often occurs on complex media [35] and there is a need to understand limb interaction with complex substrates [36]. While the scalings of such properties as penetration depth and collision time might be largely insensitive to intruder and grain geometry, the details of the force developed during penetration certainly are, and thus theory is needed to model such effects.

ACKNOWLEDGMENTS

We thank Roman Grigoriev and Robert J. Full for their comments and discussions. We also thank David Sweeney, Homero Lara, and Mateo Garcia for collecting data as well as Lionel London for photographic assistance.

[1] H. J. Melosh, *Impact Cratering: A Geologic Process* (Oxford University Press, Oxford, 1989).
[2] M. Burrows and G. Hoyle, J. Exp. Biol. **58**, 327 (1973).
[3] B. Robins, *New Principles of Gunnery* (J. Nourse, London, 1742).
[4] M. P. Ciamarra, A. H. Lara, A. T. Lee, D. I. Goldman, I. Vishik, and H. L. Swinney, Phys. Rev. Lett. **92**, 194301 (2004).
[5] J. R. de Bruyn and A. M. Walsh, Can. J. Phys. **82**, 439 (2004).
[6] W. A. Allen, E. B. Mayfield, and H. L. Morrison, J. Appl. Phys. **28**, 370 (1957).
[7] M. J. Forrestal and V. K. Luk, Int. J. Impact Eng. **12**, 427 (1992).
[8] D. Lohse, R. Bergmann, R. Mikkelsen, C. Zeilstra, D. van der Meer, M. Versluis, K. van der Weele, M. van der Hoef, and H. Kuipers, Phys. Rev. Lett. **93**, 198003 (2004).
[9] M. Hou, Z. Peng, R. Liu, K. Lu, and C. K. Chan, Phys. Rev. E **72** 062301 (2005).
[10] Y. Boguslavskii, S. Drabkin, and A. Salman, J. Phys. D **29**, 905 (1996).
[11] A. M. Walsh, K. E. Holloway, P. Habdas, and J. R. de Bruyn, Phys. Rev. Lett. **91**, 104301 (2003).
[12] K. Wada, H. Senshu, and T. Matsui, Icarus **180**, 528 (2006).
[13] W. A. Allen, E. B. Mayfield, and H. L. Morrison, J. Appl.

Phys. **28**, 1331 (1957).
[14] L. S. Tsimring and D. Volfson, in *Powders and Grains 2005*, edited by R. García-Rojo, H. J. Herrmann, and S. McNamara (A. A. Balkema, Rotterdam, 2005), Vol. 2, pp. 1215–1223.
[15] M. A. Ambroso, R. D. Kamien, and D. J. Durian, Phys. Rev. E **72**, 041305 (2005).
[16] M. A. Ambroso, C. R. Santore, A. R. Abate, and D. J. Durian, Phys. Rev. E **71**, 051305 (2005).
[17] M. B. Stone, R. Barry, D. P. Bernstein, M. D. Pelc, Y. K. Tsui, and P. Schiffer, Phys. Rev. E **70**, 041301 (2004).
[18] H. Katsuragi and D. J. Durian, Nat. Phys. **3**, 420 (2007).
[19] D. Lohse, R. Rauhé, R. Bergmann, and D. van der Meer, Nature (London) **432**, 689 (2004).
[20] S. T. Thoroddsen and A. Q. Shen, Phys. Fluids **13**, 4 (2001).
[21] R. M. Nedderman, *Statics and Kinematics of Granular Materials* (Cambridge University Press, Cambridge, U.K., 1992).
[22] D. Tritton, *Physical Fluid Dynamics* (Oxford University Press, Oxford, 1989).
[23] D. Howell, R. P. Behringer, and C. Veje, Phys. Rev. Lett. **82**, 5241 (1999).
[24] B. Miller, C. O'Hern, and R. P. Behringer, Phys. Rev. Lett. **77**, 3110 (1996).
[25] K. E. Daniels, J. E. Coppock, and R. P. Behringer, Chaos **14**, S4 (2004).
[26] M. Schröter, S. Nagle, C. Radin, and H. L. Swinney, Europhys. Lett. **78**, 44004 (2007).
[27] D. I. Goldman and H. L. Swinney, Phys. Rev. Lett. **96**, 145702 (2006).
[28] J. Jenkins and M. Richman, Arch. Ration. Mech. Anal. **87**, 355 (1985).
[29] C. S. Campbell, Annu. Rev. Fluid Mech. **22**, 57 (1990).
[30] E. C. Rericha, C. Bizon, M. D. Shattuck, and H. L. Swinney, Phys. Rev. Lett. **88**, 014302 (2001).
[31] J. Bougie, Sung Joon Moon, J. B. Swift, and H. L. Swinney, Phys. Rev. E **66**, 051301 (2002).
[32] D. Volfson, L. S. Tsimring, and I. S. Aranson, Phys. Rev. E **68**, 021301 (2003).
[33] U. Saranli, M. Buehler, and D. E. Koditschek, Int. J. Robot. Res. **20**(7), 616 (2001).
[34] P. Holmes, R. J. Full, D. Koditschek, and J. Guckenheimer, SIAM Rev. **48**, 207 (2006).
[35] K. Autumn *et al.*, in *Unmanned Ground Vehicle Technology VII*, edited by D. W. G. Grant, R. Gerhart, and Charles M. Shoemaker, Proceedings of SPIE Vol. 5804 (SPIE, Bellingham, WA, 2005), pp. 291–302.
[36] J. P. Spagna, D. I. Goldman, P.-C. Lin, D. E. Koditschek, and R. J. Full, Bioinspiration Biomimetics **2**, 9 (2007).